applied sciences

MDPI

Article

Light Scattering from Small Clusters of Chiral and Symmetric Particles: Shape-Dependent Analysis

Yehor Surkov [1], Yuriy Shkuratov [2], Karri Muinonen [1], Antti Penttilä [1], Vadym Kaydash [2], Yongxiang Hu [3], Yong-Le Pan [4], Chuji Wang [5,6] and Gorden Videen [6,7,8,*]

1 Department of Physics, University of Helsinki, P.O. Box 64, FI-00014 Helsinki, Finland; yehorsurkov@gmail.com (Y.S.); karri.muinonen@helsinki.fi (K.M.); antti.i.penttila@helsinki.fi (A.P.)
2 Institute of Astronomy, V.N. Karazin Kharkiv National University, Svobody Square 4, 61022 Kharkiv, Ukraine; yuriy.shkuratov@gmail.com (Y.S.)
3 Science Directorate, NASA Langley Research Center, Hampton, VA 23681, USA
4 DEVCOM Army Research Laboratory, Adelphi, MD 20783, USA
5 Department of Physics and Astronomy, Mississippi State University, Starkville, MS 39759, USA; cw175@msstate.edu
6 Space Science Institute, 4765 Walnut Street, Suite B, Boulder, CO 80301, USA
7 Department of Atmospheric Sciences, Texas A&M University, College Station, TX 77843, USA
8 Humanitas College, Kyung Hee University, Yongin 02447, Republic of Korea
* Correspondence: gorden.videen@gmail.com

Featured Application

The aim of this study is to provide information on the use of CIDS as an optical tool to differentiate chiral from non-chiral particles. CIDS has been proposed as a remote-sensing tool to detect the presence of biological and prebiotic materials.

Abstract

We present a numerical study comparing light scattering by small clusters composed of helices, capsules, and spheres. Using the discrete-dipole approximation (DDA), we compute orientation-averaged Mueller-matrix elements M_{11}, M_{12}, and M_{14} for clusters with varying number of monomers (N = 5–45) and mean center-to-center separation (1–10 particle diameters). Our analysis isolates the influence of particle morphology on angular scattering intensity, linear polarization, and circular intensity differential scattering (CIDS), providing a direct comparison of symmetric and chiral shapes. Helices display persistent angular fine structure in M_{11} and deep, side-scattering maxima in M_{12}, while spheres and capsules converge to smoother polarization curves with increasing separation. CIDS from symmetric monomers manifests as small oscillations around zero that decay rapidly with monomer separation and number. In contrast, helices produce a stable backward CIDS slope that is largely separation-independent but gradually flattens with increasing number of monomers. These trends confirm that morphology alone can influence key polarization characteristics and provide insights for interpreting scattering from complex-shaped particles. Such morphology-related features may help in the interpretation of polarization data in aerosol and planetary remote sensing and justify the refinement of the design of optical setups for studying irregular or chiral particles in controlled environments.

Keywords: light polarization; Mueller matrix; CIDS; chirality

Check for updates

Academic Editor: Alexander Zhbanov

Received: 5 November 2025
Revised: 16 December 2025
Accepted: 5 January 2026
Published: 14 January 2026

Copyright: © 2026 by the authors. Licensee MDPI, Basel, Switzerland. This article is an open access article distributed under the terms and conditions of the Creative Commons Attribution (CC BY) license.

1. Introduction

The emergence of circular polarization in scattered light serves as evidence of a break in spatial symmetry, either of the physical (e.g., the presence of magnetic fields or magnetization), optical (e.g., anisotropy of refractive index in solids or optical activity of chiral molecules), or geometric properties (e.g., the presence of a chiral arrangement of the material) of the studied object. Chirality is associated commonly with components having a biological origin. This characteristic has broad applications in various biomedical studies [1–3], remote sensing of Earth's atmosphere [4–6] and potentially habitable planets and moons in the Solar System [7–9].

One of the most intriguing turns in the history of circular polarization research was the discovery of its presence in comet studies [10,11], since it had been theoretically shown that for media consisting of a sufficiently large number of particles containing both particles and their mirror images, circular polarization equals zero [12,13]. As the surface of comets apparently possesses neither sufficient magnetization nor a widespread abundance of complex organic molecules having chiral properties, this discovery initiated an intensive search for other possible mechanisms, primarily related to the light-scattering properties, responsible for this effect. Thus, in theoretical [14–18], experimental, and observational studies [19–21], it was found that circular polarization can arise from light scattering by objects consisting of particles that do not possess a chiral form but are arranged sufficiently asymmetrically.

A practical interest arises in distinguishing the circular polarization of media resulting from light scattering by objects of asymmetric form from the component associated with other violations of the symmetry of the geometric characteristics of the medium. This would allow for the improvement of modern methods of remote sensing of objects for the presence of a biological component, for example, bioaerosols in the study of transmission pathways of infectious diseases [22,23] or in the search for the presence of life on the satellites of planets within our Solar System and in exoplanets [24,25].

In this study, we investigate light scattering by clusters composed of identical monomers in the shapes of helices, capsules, and spheres (Figure 1). The primary objective is to examine the behavior of key light-scattering parameters, such as intensity, linear polarization, and circular polarization, for clusters of chiral and non-chiral monomers, and to analyze their dependence on the main geometric characteristics of these clusters (e.g., interparticle distance and particle number), without focusing on specific examples of such objects in nature. It is worth noting that the choice of these shapes is inspired by the morphological classification of major bacterial types (spherical cocci, capsule-shaped bacilli, and helical spirilla). Additionally, the selected chiral form, the helix, is one of the most fundamentally widespread shapes characterizing living matter.

Despite significant advancements in computational power, direct modeling of light scattering in media composed of a large number of morphologically complex objects remains a challenging and time-consuming task. Therefore, we focus on the study of clusters with a comparatively small number of monomers. To identify potentially more universal properties that are, to some extent, independent of the specific spatial arrangement of the monomers composing each cluster, we perform orientation averaging of the Mueller matrix and concentrate on characteristics that are most convenient for experimental measurements: intensity, linear polarization, and circular polarization. These properties are conveniently expressed through the corresponding Mueller-matrix elements. Specifically, the phase dependence of the M_{11} element directly provides the angular intensity distribution, or scattering indicatrix (phase function). The linear polarization is expressed using the Mueller-matrix elements according to the widely used notation $P_L = -Q/I = (I_\perp - I_{||})/(I_\perp + I_{||}) = -M_{12}/M_{11}$, where I and Q are the first and the second Stokes parameters, respectively. The Stokes vector is defined as

$S = [I, Q, U, V]^T = [I_{||} + I_{\perp}, I_{||} - I_{\perp}, I_{\pi/4} - I_{-\pi/4}, I_R - I_L]^T$ (e.g., [26]). The circular polarization properties of the modeled clusters are characterized by the circular intensity differential scattering (CIDS), defined as $CIDS = -V/I = (I_L - I_R)/(I_L + I_R) = -M_{14}/M_{11}$, where the Stokes vectors for incident right- and left-circularly polarized light are assumed to be $[1, 0, 0, 1]^T$ and $[1, 0, 0, -1]^T$, respectively [4,26].

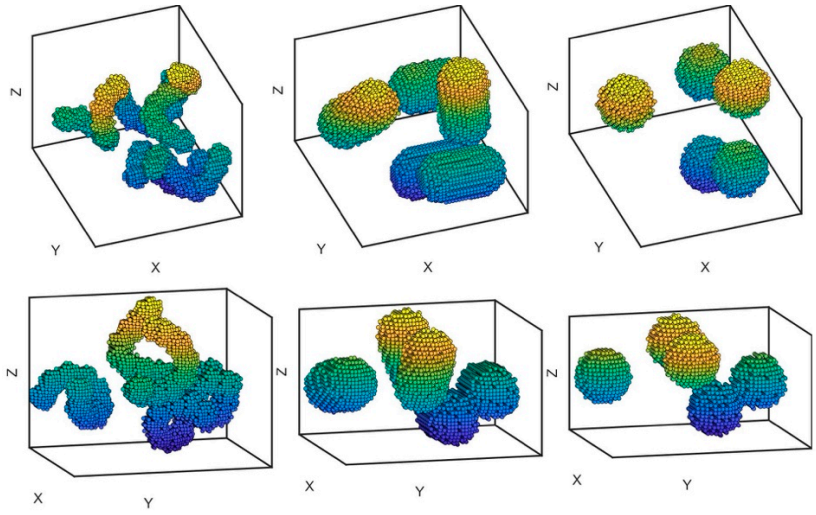


Figure 1. Densely packed clusters of monomers with helical, capsule, and spherical shapes. Particles can touch each other without intersection. All monomers share the same position of central points (for helices, the central point is outside of a particle volume). Helical and capsule monomers have the same directions of main axes as well.

To characterize the differences caused by the asymmetric arrangement of monomers with symmetric shapes and the effects arising from the asymmetric shape of an individual monomer, we limit our investigation to clusters of monomers whose centers coincide across all shapes and are arranged asymmetrically. During orientation averaging, the entire cluster is rotated while preserving the relative positions and orientations of the monomers within it.

2. Materials and Methods

As demonstrated by Kolokolova et al. [14,15], the collective scattering properties of particle clusters depend on their number, positions, and mutual orientation. In this study, we additionally consider the packing density parameter and the average distance between monomers. All clusters examined here consist of from 5 to 45 monomers. Unlike the work of Guirado et al. [17] in which the clusters of spheres strictly represent chiral shapes, referred to as "chiral snake particle" and "Mr. Sanchez", in our research, the particles are arranged randomly in such a way that their configuration exhibits chirality. This means that the clusters cannot be superimposed onto their mirror images through simple geometric transformations such as rotation or translation. Examples of the studied clusters are shown in Figure 2. All helices have the same handedness. For the clusters shaped as elongated helices and capsules, the relative orientations of particle axes, in addition to the alignment of their geometric centers, are also preserved.

Light scattering is significantly influenced by particle morphology. It is desirable to characterize common geometric properties of the selected particles, but due to the nature of the particles we consider only the most basic spatial characteristics are in common. Therefore, in selecting the geometric characteristics, we based our approach on a chiral helix, for which, upon averaging over orientations, stronger circular polarization across

a wide range of values for the imaginary part of the refractive index were achieved when the helix length ranged from one to several wavelengths [27].

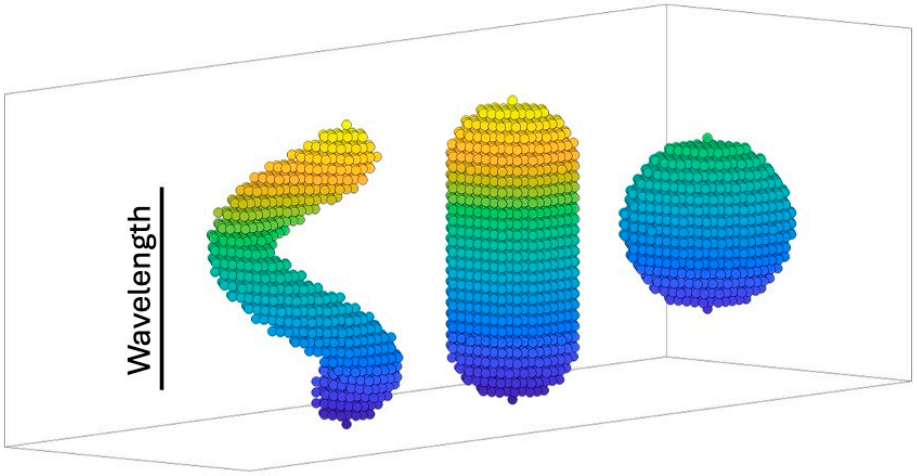


Figure 2. Graphical representation of the discretized monomer shapes used in the cluster models. The black vertical line corresponds to one wavelength.

In this study, we model clusters composed of three particle types: helices, capsules, and spheres. The helical particles are represented by a one-turn helix with a total length of 1.5 λ, a mean radius equal to 0.25 of the helix length (i.e., 0.375 λ), and a tube radius equal to 1/8 of the helix length (i.e., 0.1875 λ). This geometry produces sufficiently high values of orientation-averaged circular polarization. Nevertheless, this configuration was chosen empirically, and other helical shapes, differing in length, radius, or pitch, may yield either stronger or weaker CIDS signals depending on their structural and optical parameters. The capsule-shaped particles are assigned a total length of 1.5 λ, with the radius of the generating cylinder set equal to the helix mean radius (0.375 λ). The spherical particles have a radius equal to 0.3 of the helix length, which corresponds to 0.45 λ. The graphical representation of these shapes is shown in Figure 2. A uniform refractive index of m = 1.6 + 0.001i is used for all particles throughout the study.

The effect of cluster porosity on light scattering by such configurations is studied for two cases: (1) a fixed number of particles but varying average distances between monomers (Figure 3a–c), and (2) a fixed average distance but varying numbers of particles (Figure 3d–f). For a non-discrete random arrangement of particles in a cluster, the concept of average distance is not well-defined. Therefore, in this work, the average distance refers to the value specified during the construction of the corresponding cluster.

The cluster construction is performed as follows. In the case of helices and capsules, the position and orientation of the initial particle is specified. Then, subsequent particles are added at a distance equal to the size parameter, with an unfixed position and orientation. For each added monomer, we check to ensure no overlap with previously placed monomers. The generation of clusters with a large number of monomers can take a considerable amount of time. Therefore, instead of using a fixed distance to the next one, a random value is employed, represented by a Gaussian distribution with a mean equal to the modeled distance and a standard deviation equal to one-quarter of the modeled distance. Additionally, for the generated configurations, the average distance to the two nearest neighbors is calculated for each monomer and then averaged across the cluster, and only those clusters where this average distance does not deviate from the desired spacing by more than 0.5 of the circumscribed sphere diameters are retained. Thus, the distance referred to later in the text as the “mean distance” or “interparticle distance” is a controlled construction parameter rather than a strict geometric average.

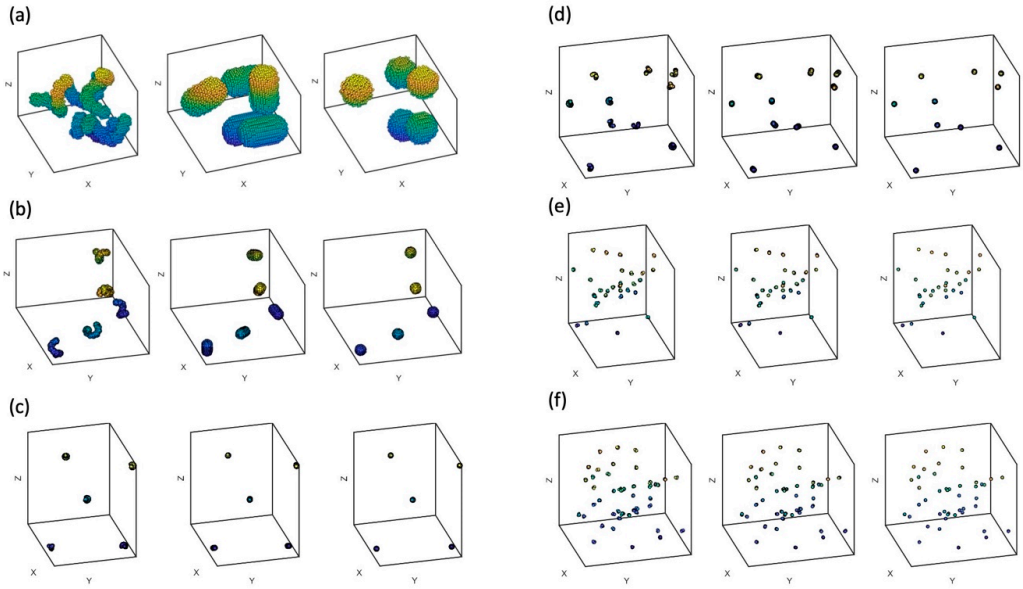


Figure 3. The clusters are characterized in this work by the mean distance between monomers (**a**–**c**) and their number in the cluster (**d**–**f**). From left to right, particle types are helices, capsules, and spheres. Figures (**a**–**c**) show the clusters of five monomers with mean distances between their centers of 1, 3, and 10 diameters of the circumscribed sphere about the helical particle, respectively. Clusters with the mean distance of 5 diameters with different numbers of monomers (10, 30, and 45) are presented in figures (**d**–**f**).

This random-placement method inherently produces configurations that almost surely contain chiral subsets, due to the lack of imposed symmetry in the particle positions. To explicitly confirm the presence of chirality, each generated cluster was analyzed using the Kabsch algorithm, which finds the optimal rotation that aligns a mirrored configuration to the original. For each cluster, subsets of positions of 4 monomers were sequentially tested until at least one tetrahedron was confirmed to be chiral; in practice, this detection typically occurs after checking only one or two tetrahedra. Ultimately, only clusters satisfying both the spacing condition and the presence of chiral subsets were retained for modeling. This procedure ensures that the final clusters not only respect realistic monomer spacing but also contain guaranteed chiral structures, providing a suitable basis for subsequent light-scattering simulations.

Examples of clusters generated with 5 monomers with distance parameters of 1, 3, and 10 diameters of the circumscribed spheres about the helical particles are shown in Figure 3a–c. We use the helical-particle circumscribed sphere's diameter as a measure of distance because we would like to keep the particle densities the same for comparison, and the helical-particle circumscribed sphere is the largest. If we were to use a smaller circumscribed sphere, there would be osculation for the helical particles, which we want to avoid. In cases with a small number of monomers, the pairwise distances between the nearest particles are relatively uniform. However, as the number of particles in the cluster increases, the more compact groups of particles and particles scattered at distances significantly larger than the average distance can form. This study is not restricted to cases with uniform particle distributions for clusters of larger particle numbers. The only prohibition of all considered clusters is non-overlapping that was checked with discretized shapes and not with circumscribed spheres.

To compute the orientation-averaged Mueller-matrix elements, we use the DDA method [28]. Although this method is computationally demanding, which imposes limitations on the size and number of particles in the studied clusters, its advantage is the ability to model particles with complex shapes. Specifically, this method enables the creation and

investigation of clusters composed of arbitrary shapes, including chiral particles, in our case, helices, rather than clusters consisting of simpler shapes arranged in a chiral manner.

The essence of the DDA method lies in approximating the particle's shape using a discrete set of voxels that are small compared to the wavelength. The geometry of their arrangement characterizes the particle shape, while their microphysical properties, specifically their polarizabilities, determine the optical properties of the material. Calculating scattering by such a system involves solving a large system of algebraic equations, where the scattered field is the cumulative field from all voxels. This field is calculated within the Rayleigh approximation, accounting for the fact that each individual dipole interacts with both the incident wave field and the scattered field from all other dipoles in the system. For the numerical solution of the scattering problem, we use the ADDA software package [29,30] to compute Mueller-matrix elements averaged over orientation for the clusters.

When discretizing the particles into voxels, we employ a discretization parameter corresponding to 20 dipoles per wavelength in the medium. This choice satisfies the general requirement for optimal selection $N > 10\,|m|$ [31]. The increase in this parameter beyond the optimal value in this study is dictated by the need for a more accurate representation of the helical shapes with the specified geometric parameters. To convert the macroscopic optical parameter of the complex refractive index to the microscopic polarizability of the voxels, we use the LDR polarizability model [28].

Orientation averaging in ADDA was performed over the three Euler angles (α, β, γ) using its adaptive Romberg integration, which refines the angular grid until the desired accuracy is reached [29,30]. The angle α was treated as periodic over 0–360° (with the grid spacing boundaries $J_{\min} = 2$, $J_{\max} = 5$), while β (0–180°) and γ (0–360°) were sampled on gradually refined grids that each required full DDA evaluations. We applied default ADDA parameters for orientation averaging [30]. According to the ADDA log files, both the inner and outer integrations converged, confirming that the results should represent a stable orientation-averaged solution.

Since the objective of this study was not initially to compare the computational results with light-scattering experiments for any specific objects, the control of correctness and evaluation of computational accuracy were performed based on the presence of certain symmetries in the orientation-averaged Mueller-matrix elements. For all the matrices presented below, the following inequalities hold true: $<(M_{12} - M_{21})/M_{11}>$ is less than 0.005; $<(M_{14} - M_{41})/M_{11}>$ is less than 0.005; $<(M_{34} + M_{43})/M_{11}>$ is less than 0.005, which must hold for any orientationally averaged finite system. Here, <. . .> denotes the arithmetic averaging of the values over the scattering angles, and M_{ij} are the corresponding elements of the Mueller matrices of the clusters, averaged over orientation.

Another issue was checked. As helices are the key shape in our analysis, having strongly curved surfaces makes them particularly sensitive to the discretization level. We additionally verified the stability of the particle discretization. Using 20 dipoles per wavelength ensures a sufficient number of dipoles to represent the material's optical properties, but it does not necessarily guarantee accurate shape representation. Figure 4 presents the orientation-averaged Mueller-matrix elements for a single helical particle and for a cluster of five monomers separated by an average distance of 10 circumscribed sphere diameters, computed with discretization values of 20 and 30 dipoles per wavelength. For the single-particle case, the agreement between the two discretizations is good, with differences increasing only slightly in the backward direction for both the angular intensity distribution (M_{11}) and the CIDS parameter ($-M_{14}/M_{11}$). For the cluster case, the results also show satisfactory agreement, preserving the overall angular trends and exhibiting only minor, though noticeable, deviations in the comb-like pattern. Aiming to investigate

only the general characteristics and patterns, we consider a discretization of 20 dipoles per wavelength to be sufficient for the purposes of the present study.

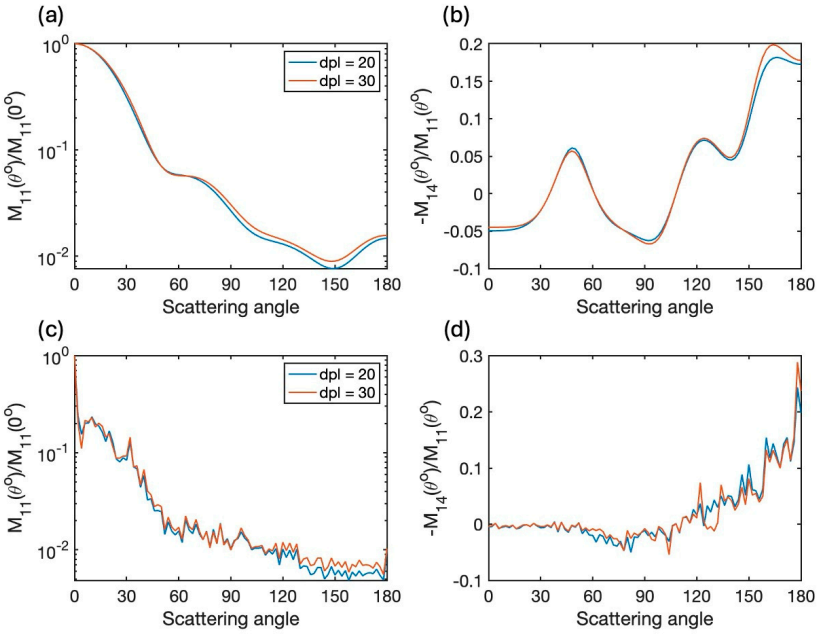


Figure 4. Panels (**a**,**b**) show the orientation-averaged Mueller-matrix element M_{11}, normalized to its exact forward value, and the ratio M_{14}/M_{11} for two discretization levels, 20 and 30 dipoles per wavelength, for a single helix. Panels (**c**,**d**) present the same quantities for a cluster of five monomers with a mean inter-monomer distance of 10 circumscribed sphere diameters. The notation "dpl" denotes the number of dipoles per wavelength, preserved as in the original ADDA parameter list.

3. Results

The orientation-averaged angular dependencies of the Mueller-matrix elements $M_{11}(\theta)/M_{11}(0)$, $-M_{12}(\theta)/M_{11}(\theta)$, and $-M_{14}(\theta)/M_{11}(\theta)$ are shown in Figures 5 and 6 for a single particle and clusters composed of five monomers separated by 1, 3, and 10 circumscribing-sphere diameters. The grouping highlights the interparticle distance (Figure 4) and the particle type (Figure 5).

For single-particle scattering, the normalized angular intensity distributions $M_{11}(\theta)/M_{11}(0)$ show features typical of the studied particle sizes: all exhibit a deep minimum at scattering angles between 130° and 150°, about two orders of magnitude below the forward-scattering peak. Helices are the only shape that introduce additional features near 45–50° and 100°. Increasing the separation between monomers produces a strong, narrow interference peak in the forward direction, while the overall features at larger phase angles are retained. Spheres preserve the pronounced minimum at ~150°; whereas, for capsules and helices, the angular distributions flatten as separation increases.

Linear polarization, expressed as $-M_{12}(\theta)/M_{11}(\theta)$, exhibits a stronger dependence on particle shape. For spheres and capsules, the angular variation follows the simple pattern characteristic of small particles, with a single maximum and minimum (Figure 3a). Helices, in contrast, produce a more complex dependence with multiple extrema. For single particles, capsules broadly resemble spheres, but their extremal values approach those found for helices. The helical results for a single particle are consistent with earlier work on one-turn helices [27], with the present geometry (radius doubled relative to that of the previous work) yielding slightly larger extrema (0.26 vs. 0.17) and shifting them by ~30° to larger scattering angles, while preserving the same number and configuration of extrema. For helical clusters, the phase dependence differs strongly from the single-particle case: closely packed helices generate a bell-shaped dependence with a maximum approaching 1

(complete linear polarization) near 90–95°, and this profile remains essentially unchanged as the separation increases (Figure 3b–d).

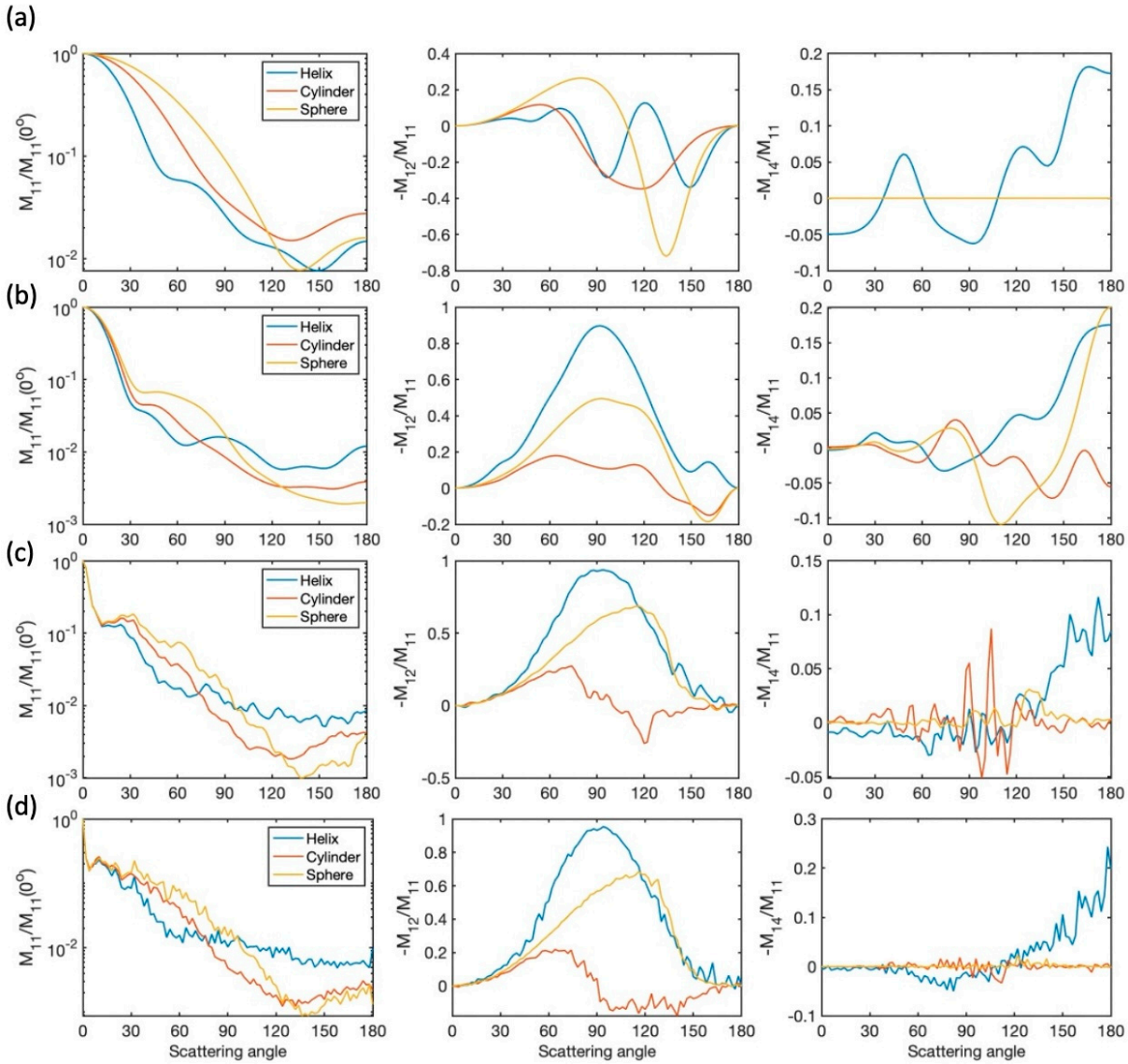


Figure 5. The angular dependencies of indicatrices normalized to the forward direction $M_{11}(\theta)/M_{11}(0)$ (left column), the linear polarization characteristics $-M_{12}(\theta)/M_{11}(\theta)$ (middle column), and the $CIDS = -M_{14}(\theta)/M_{11}(\theta)$ (right column) are shown for (**a**) a single particle and clusters of five monomers with mean separation distances equal to (**b**) 1, (**c**) 3, and (**d**) 10 diameters of the spheres circumscribed about the individual helices.

As expected from earlier studies [14–18], asymmetric arrangements of closely packed, symmetric monomers produce noticeable circular polarization, expressed as $-M_{14}(\theta)/M_{11}(\theta)$, with amplitudes comparable to those of chiral helices. However, this effect diminishes rapidly once the interparticle distance exceeds several diameters of the circumscribed sphere. By contrast, helices maintain a systematic backward-hemisphere trend, even at large separations. This distinction highlights two mechanisms for circular polarization: interference-driven effects in symmetric aggregates as well as the intrinsic chirality of helices.

When grouped by particle type (Figure 6), the angular dependencies illustrate these differences clearly. For intensity $M_{11}(\theta)/M_{11}(0)$, the ~150° minimum is preserved only for spheres, while capsules and helices develop flatter distributions as separation increases. For linear polarization, capsules occupy an intermediate position between spheres and helices,

with helices displaying the most stable and distinctive profiles. Circular polarization for spheres and capsules is weak and oscillatory, with amplitudes typically of only a few percent and strongly dependent on configuration. Helices, on the other hand, generate a smooth, slope-like dependence in the backward direction that is largely unaffected by monomer separation.

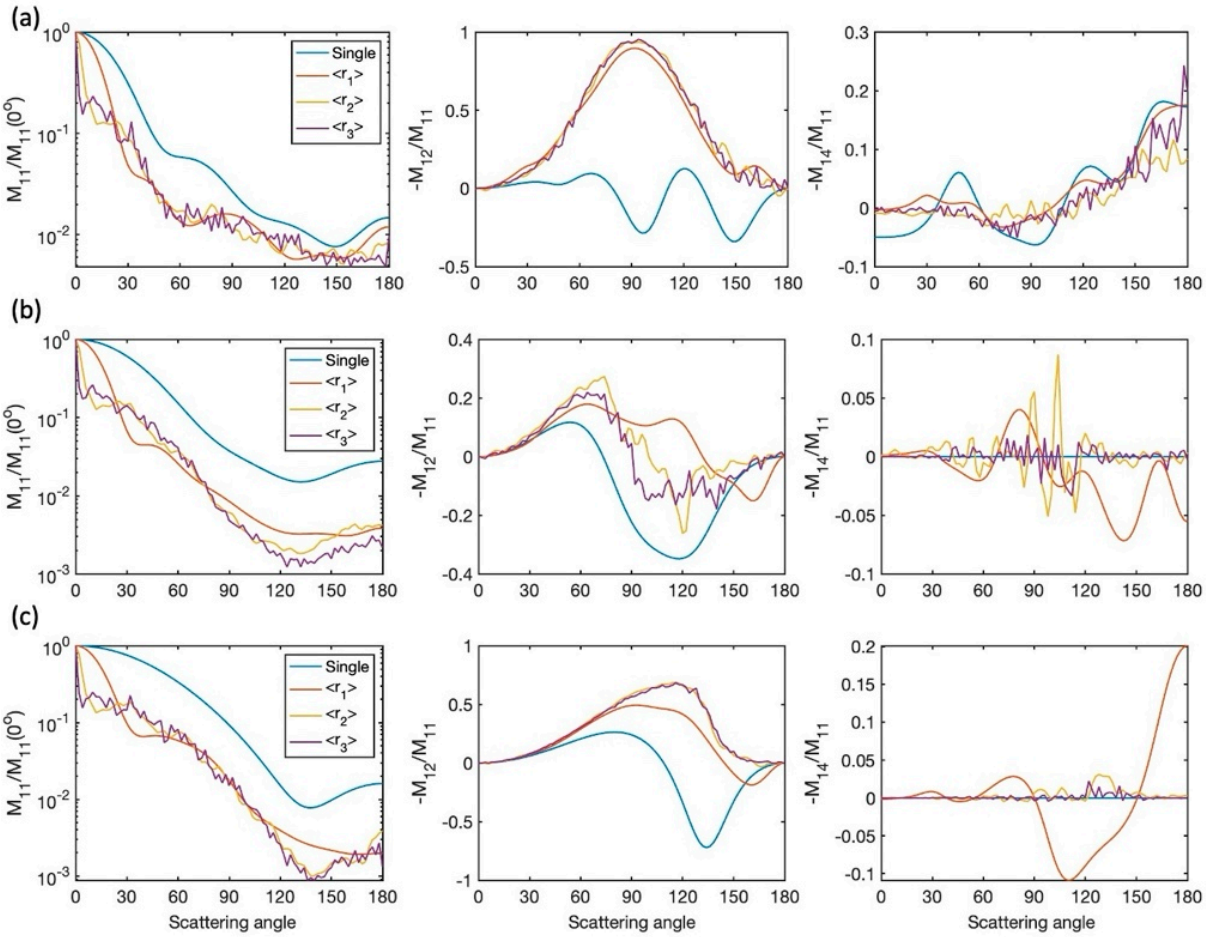


Figure 6. The angular dependencies of indicatrices normalized to the forward direction $M_{11}(\theta)/M_{11}(0°)$ (left column), the linear polarization characteristics $-M_{12}(\theta)/M_{11}(\theta)$ (middle column), and the $CIDS = -M_{14}(\theta)/M_{11}(\theta)$ (right column) are shown for the same orientation of 5-particle clusters composed of (**a**) helices; (**b**) capsules; (**c**) spheres. The mean distances between monomers are equal to $\langle r_1 \rangle = 1$, $\langle r_2 \rangle = 3$, and $\langle r_3 \rangle = 10$ of the diameter of a circumscribing sphere about the monomers.

Taken together, Figures 5 and 6 present a coherent picture of how monomer separation and particle morphology govern scattering. Figure 3 highlights how interference effects dominate at short separations but vanish at larger ones, especially in the forward direction. Figure 6 underscores the persistence of shape-controlled features. The results for circular polarization further reinforce this distinction: symmetric particles yield only weak, arrangement-induced oscillations that disappear with increasing cluster sparseness, whereas helices produce robust, slope-like dependencies that persist across all separations.

Figures 7 and 8 show the orientation-averaged angular dependencies of the Mueller-matrix elements for clusters composed of $N = 15$, 30, and 45 monomers. The monomers are separated by an average distance of five diameters of the circumscribed spheres, and the entire clusters are rotated during averaging. For clarity, the results are organized in two ways: by particle number (Figure 7) and by particle type (Figure 6), consistent with the grouping used earlier for Figures 5 and 6.

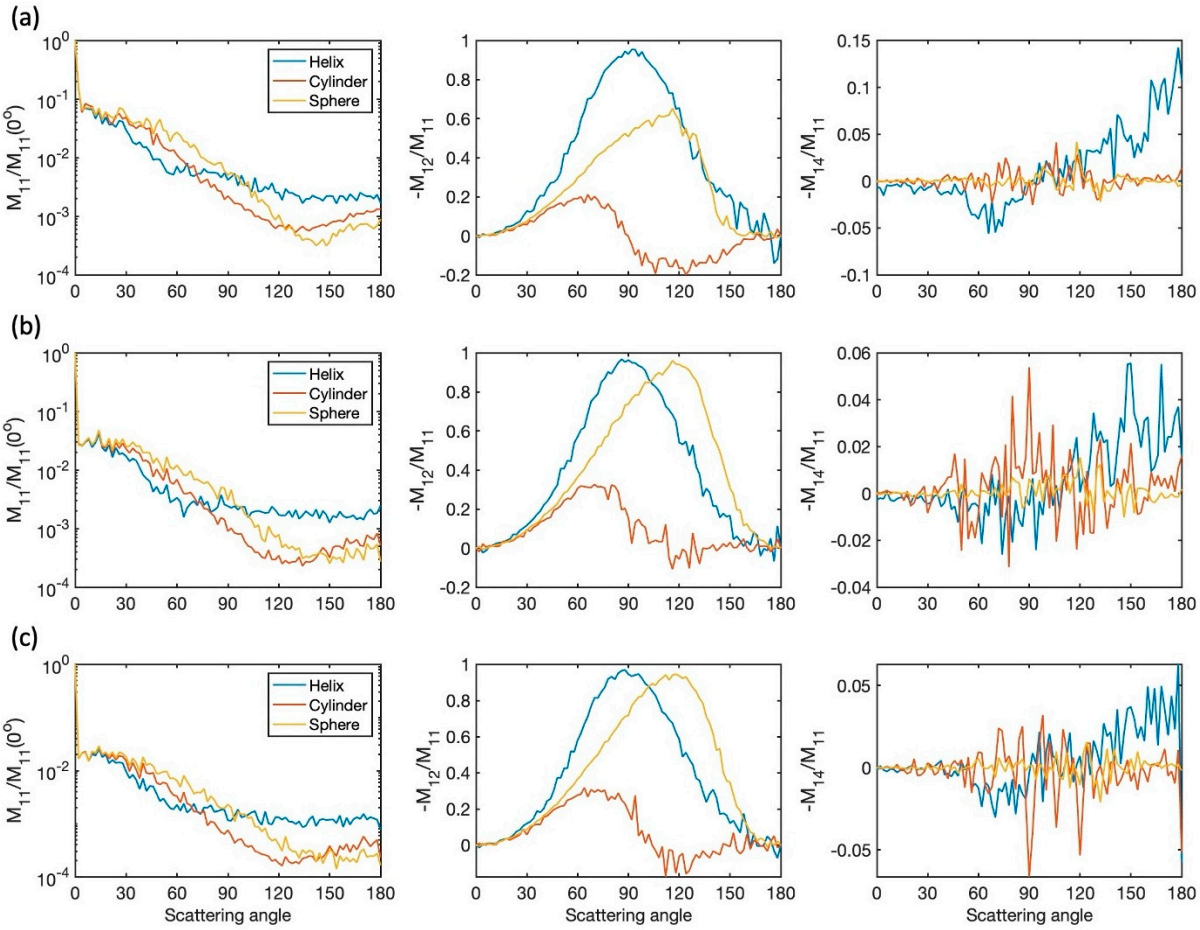


Figure 7. The angular dependencies of indicatrices normalized to the forward direction $M_{11}(\theta)/M_{11}(0^\circ)$, the linear polarization characteristics $-M_{12}(\theta)/M_{11}(0^\circ)$ and $CIDS = -M_{14}(\theta)/M_{11}(\theta)$ are shown for the clusters composed of different numbers of monomers N = (**a**) 15, (**b**) 30, and (**c**) 45.

The influence of particle number on the normalized scattering intensity $M_{11}(\theta)/M_{11}(0^\circ)$ is relatively weak when monomers are separated by several diameters (Figure 7a). The main effect is confined to the forward-scattering lobe, where the height and width of the interference peak increase with N. This trend most likely reflects the growth of the effective cluster size rather than a direct effect of particle number, as a larger system has a larger cross-section. At scattering angles larger than ~10–20°, the intensity profiles converge, indicating that morphology rather than particle count governs the angular behavior. Linear polarization $-M_{12}(\theta)/M_{11}(\theta)$ shows more noticeable differences: for spheres and capsules, the extrema decrease as N increases from 15 to 30, but the curves for N = 30 and N = 45 are nearly indistinguishable. Helices, by contrast, show essentially no dependence on particle number, suggesting a dominance of morphology over cluster size. For circular polarization $M_{14}(\theta)/M_{11}(\theta)$, oscillations around zero are visible for spheres and capsules, while helices show a slope-like downward trend starting from 60 to 70°, consistent with single-helix results. With increasing N, the oscillatory signals for symmetric particles are smoothed by averaging, whereas the helical slope flattens gradually but remains present.

When grouped by morphology, the angular dependencies illustrate the contrast between spheres, capsules, and helices more clearly (Figure 8). For intensity $M_{11}(\theta)/M_{11}(0^\circ)$, the forward-scattering peak grows with particle number, but beyond ~20° the curves for a given shape largely coincide, confirming that particle type dominates the angular dependence (Figure 8a). Linear polarization (Figure 8b) shows that spheres and capsules preserve recognizable single-particle features, including the number and position of extrema, while

helices produce distinctly different profiles that deviate strongly from the single-particle case. Notably, the helical curves remain essentially unchanged with increasing N, underscoring the robustness of morphology-driven polarization. For circular polarization, spheres and capsules generate only weak oscillations (±1–2%, occasionally up to 5%) that decrease as N grows, while helices consistently display the backward-hemisphere downward slope. The slope becomes shallower in larger clusters, indicating partial cancelation when many helices are combined, but it is never eliminated.

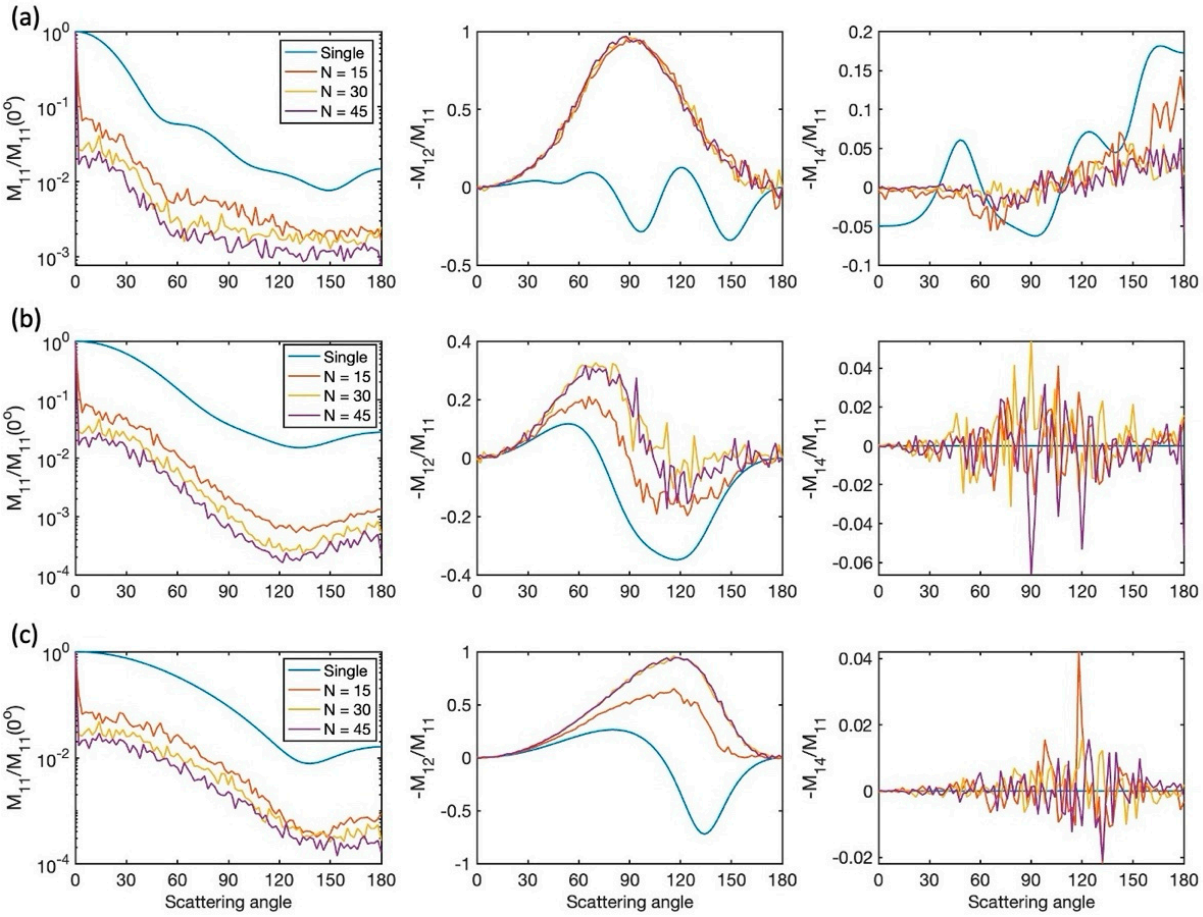


Figure 8. From left to right: the angular dependencies of indicatrices normalized to the forward direction $M_{11}(\theta)/M_{11}(0^\circ)$, the linear polarization characteristics $-M_{12}(\theta)/M_{11}(\theta)$ and $CIDS = -M_{14}(\theta)/M_{11}(\theta)$ are shown for clusters with different numbers of particles for the same shape: (**a**) helices, (**b**) capsules, and (**c**) spheres.

Together, Figures 7 and 8 clarify the dual roles of particle number and morphology in shaping the Mueller-matrix elements. Increasing N primarily affects forward scattering and suppresses oscillatory features, particularly in $-M_{14}(\theta)/M_{11}(\theta)$ for symmetric shapes. Beyond the forward region, however, the angular profiles are controlled by particle morphology: spheres retain simple oscillatory patterns, capsules serve as an intermediate case, and helices generate qualitatively distinct linear and circular polarization signatures. Importantly, while arrangement-induced circular polarization diminishes as cluster size increases, shape-induced effects from helices remain much more robust across particle counts. This distinction emphasizes the fundamental difference between interference-driven polarization, which averages out in larger aggregates, and chirality-driven polarization, which persists even for extended clusters.

4. Discussion

The preliminary analysis of the results obtained in the previous section highlights the importance of studying the light-scattering properties of particles and their clusters over a wide range of scattering angles [4,32,33]. For instance, the interference peak of scattering intensity in the forward direction in the case of particle clusters carries information about their spatial-distribution characteristics, such as packing density, and is almost independent of the shape of the particles, provided that they are relatively far apart. Linear polarization demonstrates the greatest diagnostic value at scattering angles of 60–140° [34]. Meanwhile, circular polarization, represented by the CIDS $-M_{14}/M_{11}$, tends to be most prominent in the backward direction, at least for the studied type of chiral particles, i.e., helices [27].

In Figure 9, angular distributions of intensity normalized to the forward direction are shown for cases with varying distances between particles in a cluster consisting of five monomers ranging from 1 to 10 diameters of the bounding spheres, (panels a–d, respectively) and for clusters with varying numbers of particles: 1, 15, 30, and 45 monomers (panels e–h). As shown in Figure 9a–d, the forward-scattering intensity significantly differs for the different clusters of particles. As the distance increases, and the peak narrows, the differences in the normalized M_{11} element become less distinct for randomly arranged spheres, capsules, and helices. The same weak dependence of scattering intensity is confirmed in simulations of clusters with larger numbers of particles (Figure 9e–h). Formally, as the number of particles increases, the peak also narrows, which is likely due to the increase in the overall size of the sample rather than the direct effect of the number of particles. This is expected due to the Fresnel transform relationship between particle size and diffraction.

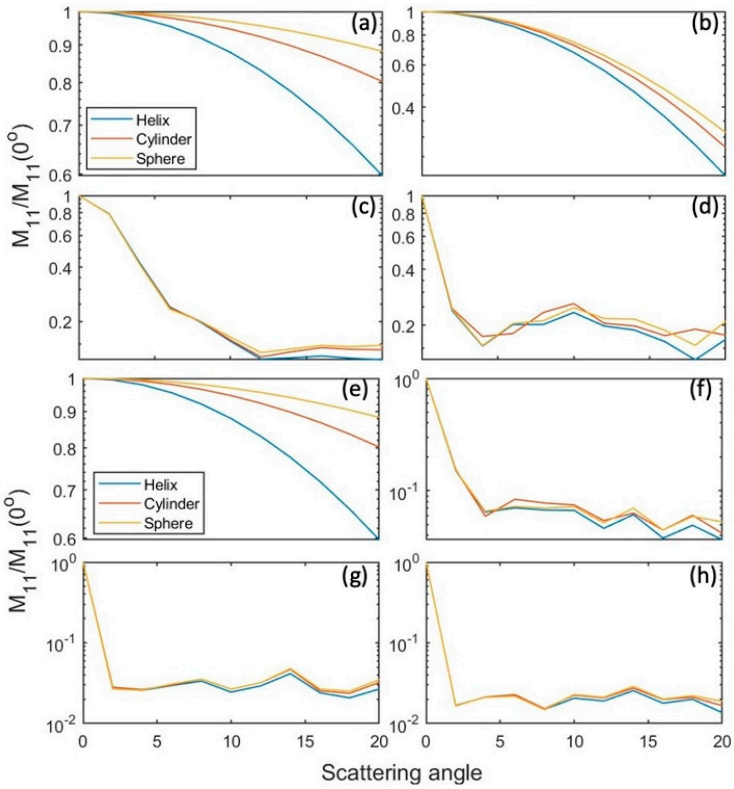


Figure 9. The angular dependencies of $M_{11}(\theta)/M_{11}(0^\circ)$ in the near-forward-scattering region for clusters consisting of five particles with different mean separation distance (**a**–**d**) and with different numbers of particles N: 1, 15, 30, and 45 (**e**–**h**).

As previously shown, circular polarization can arise both from asymmetrically arranged clusters of symmetric spheres and capsules, and from intrinsically chiral helices.

However, there is a significant difference: for symmetric shapes, the dependence of the CIDS element $-M_{14}/M_{11}$ on the scattering angle appears as oscillations around zero, which, nevertheless, can reach significant values (up to 5%) but decay relatively quickly with increasing distances between particles. The appearance and obtained values of $-M_{14}/M_{11}$ for non-symmetric clusters composed of a limited number of spherical particles are consistent with previous works [14,15,17,18], where similar arrangement-induced CIDS effects were reported. Capsules exhibit comparable trends, reaching slightly higher values of CIDS than spheres. In contrast, for the chiral helices with the investigated geometric characteristics, a relatively stable linear trend forms, starting in the backscattering direction at scattering angles exceeding 90°.

To evaluate quantitatively the effect of interparticle distance and their number on the emergence of circular polarization, the arithmetic root mean square deviation (RMSD) of $-M_{14}/M_{11}$ from zero was calculated across the entire set of scattering angles obtained from the modeling output:

$$\sqrt{\left\langle \left(-\frac{M_{14}}{M_{11}} \cdot 100\% \right)^2 \right\rangle} = \sqrt{\sum_{i=1}^{n_{sca}} \left(-\frac{M_{14}}{M_{11}} \cdot 100\% \right)^2 / n_{sca}}, \quad (1)$$

where n_{sca} is the number of scattering angles in the grid ranging from 0° to 180°, and θ_i represents the ith scattering angle in the grid. In this formula, the mean value of the parameter is neglected. This parameter was used previously [35] to characterize the impact of helical inclusions on the light scattering from liquid droplets. Unlike the maxima and minima of $-M_{14}/M_{11}$, which are extremely sensitive to specific individual configurations of the particles, this parameter tends to provide a more stable metric for comparing cluster properties across varying distances and particle numbers.

Figures 10 and 11 show the dependence of RMSD and regression slopes on interparticle distance. For spheres, the RMSD values are initially larger when particles are in close contact but decrease sharply as separation increases, nearly vanishing for clusters with separations greater than five diameters. Capsules follow a similar but less pronounced trend: their initial RMSD values are smaller but persist over a slightly wider range of distances. For helices, the situation is markedly different. The RMSD values are an order of magnitude higher (≈0.1) and remain nearly constant across the entire separation range, underscoring their robustness to dilution effects. To further characterize helices, we approximate CIDS in the range $90° \leq \theta \leq 180°$ using a linear function $CIDS_{\mathrm{fit}} = k\theta° + b$. Importantly, we do not average the Mueller matrices themselves. Instead, for each realization we compute the RMSD and the backward CIDS slope values separately, then average these derived quantities over the 10 realizations for each cluster's parameter configuration (e.g., number of monomers and interparticle distance). Thus, the trends shown in the RMSD and slope plots represent the mean behavior across the 10 cluster geometries. The variability between realizations is indicated by error bars, which represent ±3σ standard deviations.

As shown in Figure 11c for clusters of five helices, the slope is remarkably stable across monomer separations and closely matches the one obtained for the single helix. This consistency shows that the backward CIDS slopes are mostly determined by the intrinsic particle shape rather than the interactions between monomers in the cluster.

Figure 11a–c illustrate the dependence of RMSD (in the meaning of Equation (1)) and the regression slopes on the number of particles in a cluster. For spheres and capsules, increasing the number of monomers suppresses CIDS even further, reducing RMSD to near-zero values for clusters with more than ~30 particles. For helices, RMSD values remain much higher than for symmetric shapes but decrease gradually with increasing monomer number, reflecting partial cancelation of chiral effects when many randomly

oriented helices are combined. Figure 9b shows that the slope k flattens systematically as cluster size increases, and Figure 11c quantifies this trend: most of the decline occurs for $N \leq 30$, after which the slope approaches a plateau. This behavior suggests that while individual helices or small clusters of them produce strong CIDS slopes, large aggregates tend to reduce the effect without eliminating it completely.

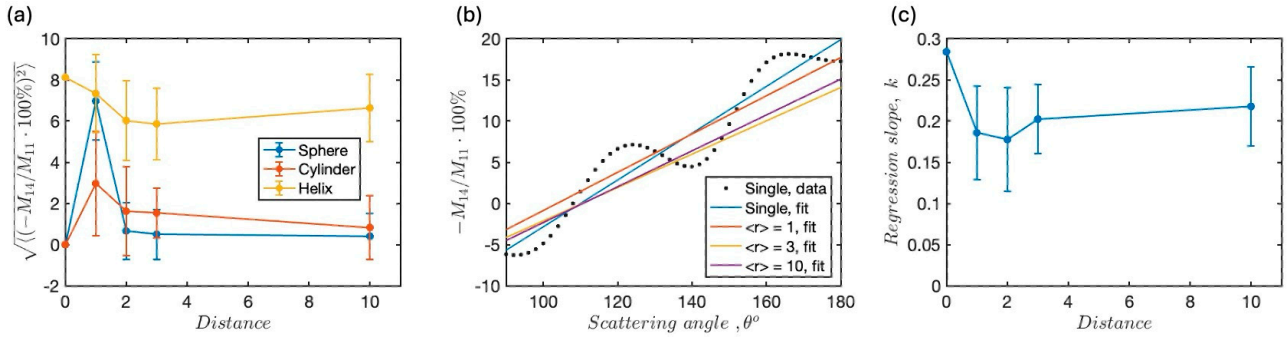


Figure 10. (**a**) Standard deviation of the $-M_{14}/M_{11}$ parameter for five monomers as a function of the average distance between particles, as a function of the diameters of the circumscribing spheres. The values of RMSD were averaged over 10 different realizations of the cluster configuration. The deviations are marked with the error bars of $\pm 3\sigma$. The negative error bar limits for this parameter are physically irrelevant and comes formally after the arithmetical subtraction. (**b**) Approximation of $-M_{14}/M_{11}$ with a linear function for helices in the scattering-angle range of 90° to 180°. (**c**) The dependence of the linear regression coefficient k from the equation $CIDS_{\text{fit}} = k\theta^{\circ} + b$, characterizing the slope of the line as a function of the mean distance between particles. The values of the slope are averaged over 10 different realizations of the cluster configuration. The deviations are marked with the error bars of $\pm 3\sigma$.

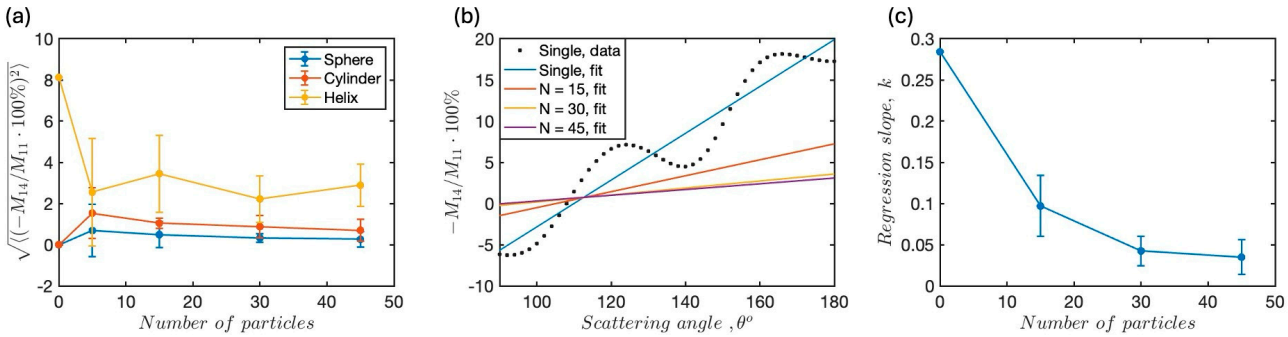


Figure 11. (**a**) Standard deviation of the $-M14/M11$ parameter for clusters of monomers with mean interparticle distance equal to five diameters of spheres circumscribed about helices as a function of the number of particles. The values of RMSD were averaged from 10 different realizations of the cluster configuration. The deviations are marked with error bars of $\pm 3\sigma$. The negative error bar limits for this parameter are physically irrelevant and appear after the arithmetical subtraction. (**b**) Results of fitting the angular dependence of $-M14/M11$ with a linear function for helical particles in the scattering-angle range of 90° to 180°. (**c**) The dependence of the linear regression coefficient k from the equation $CIDS_{\text{fit}} = k\theta^{\circ} + b$, characterizing the slope of the line as a function of the number of particles. The values of the slope are averaged over 10 different realizations of the cluster configuration. The deviations are marked with the error bars of $\pm 3\sigma$.

Together, Figures 10 and 11 highlight the distinct roles of interparticle distance and particle number. For helices, interparticle separation has little influence on either RMSD or slope, while particle number has a strong effect. For spheres and capsules, both distance and number are critical: increasing interparticle distances rapidly suppresses oscillations (Figure 10), and increasing the number of monomers further drives RMSD to zero (Figure 11).

A rigorous analytical treatment of light scattering by clusters composed of complex-shaped particles, especially in the cases of their compact emplacements, is extremely challenging. Therefore, to provide physical insight into our numerical results, we adopt a simplified approach in which M_{14} is approximated as the sum of a single-particle term and a multiple-particle coupling term:

$$M_{14} = M_{14}^{(\text{single})} + M_{14}^{(\text{multi})}, \tag{2}$$

where $M_{14}{}^{(\text{single})}$ denotes the intrinsic single-particle response, which remains nonzero after orientation averaging only for chiral particles, and $M_{14}{}^{(\text{multi})}$ arises from the interparticle coupling. The latter can be further characterized in a rough but illustrative way as follows:

$$M_{14}^{(\text{multi})} \sim \sum_{i \neq j} A_{ij} \frac{e^{\mathrm{i}kr_{ij}}}{r_{ij}^{p}}, \ (p \gtrsim 1) \sim \mathcal{O}\left(\sum_{i \neq j} r_{ij}^{-p} \, e^{\mathrm{i}kr_{ij}} \right). \tag{3}$$

Here, A_{ij} denotes the shape-, orientation-, and angular-dependent coupling coefficients, and r_{ij} are pairwise interparticle distances. Because the coefficients A_{ij} must remain finite, we can isolate the general term describing the arrangement-induced contribution to the M_{14} signal. This term contains the geometric amplitudes that decrease with separation approximately as inverse powers of interparticle distance, together with the oscillatory factors $\mathrm{e}^{\mathrm{i}kr}$. We are omitting specifying a particular power-low exponent p, since the leading-order behavior arises from far-field interference, whereas near-field terms could be stronger but more rapidly decaying.

For clusters composed of symmetric monomers, M_{14} is generated primarily by interparticle coupling, leading to a multiparticle $M_{14}{}^{(\text{multi})}$ that contains both phases $\mathrm{e}^{\mathrm{i}kr}$ and amplitudes that diminish with interparticle distance. These coupling terms therefore produce oscillatory CIDS whose magnitude decreases rapidly in amplitude as the mean separation increases. By contrast, intrinsically chiral monomers (helices) possess a nonzero single-particle chiral response $M_{14}{}^{(\text{single})}$ that survives. This results in a more persistent slope-like backward CIDS that is largely independent of spacing and is only slowly reduced as the number of monomers increases. In this case, the multiple-scattering contributions become more important, and some flattening of the slope may occur due to the accumulation of partial phase cancelation. We note that such decomposition is an extreme oversimplification. Accordingly, the interpretation offered here should be viewed as leading-order physical guidance rather than any quantitative limits. Further rigorous theoretical investigations are required to characterize CIDS behavior more fully in arbitrary multi-particle systems.

The numerical results are consistent with recent experimental findings. Laboratory studies with synthetic symmetric particles typically show only small oscillations of CIDS around zero, often close to the level of experimental uncertainty. By contrast, scattering from biological particles containing chiral components, such as DNA, spores, or pollen, produces more global angular dependencies, sometimes resembling sinusoidal or slope-dominated trends [5,36]. In synthetic systems, residual signals may arise from instrumental imperfections, small deviations from symmetry, or errors in particle positioning. In biological systems, however, more pronounced slopes likely reflect intrinsic chirality at the particle level. Although the complexity and diversity of experimentally observed CIDS patterns still make a complete, unambiguous characterization of particles challenging, even in the single-particle case, the modeling results presented above demonstrate that certain averaged or integral signatures can nevertheless provide practically useful information. In particular, the emergence of a systematic slope-like trend in the CIDS may indicate the presence of chiral components within the sampled volume, provided that the particle place-

ment is sufficiently sparse to avoid strong multiple-scattering effects. Such sparsity can often be evaluated independently, for example, through forward-scattering measurements or other a priori constraints. Importantly, these coarse but robust characteristics, like slopes, do not require full angular resolution of the scattering pattern, potentially reducing the demands put on instrument design for airborne or field-deployable detection systems. Although, the RMSD parameter remains very sensitive to angular resolution.

This connection is especially relevant because chirality is a fundamental and nearly universal feature of biological matter: amino acids or nucleic acids all possess inherent handedness and therefore break mirror symmetry in predictable ways. Consequently, chiral scattering signatures, such as the monotonic backward CIDS slope observed in helical monomers, may serve as qualitative indicators of biological content in mixed or unknown aerosol samples. While such trends are not unique fingerprints of specific species and cannot replace detailed spectroscopic or morphological characterization, they may still enable rapid screening, early warning, or coarse estimates in practical detection scenarios, especially in remote sensing in which other.

5. Conclusions

We investigated the light-scattering properties of clusters composed of non-chiral particle shapes, such as spheres and capsules, as well as chiral helices, investigating the effects of interparticle distance and the number of particles, under the condition of chiral particle arrangement within the cluster. Scattering characteristics were expressed through the Mueller-matrix elements M_{11}, M_{12}, and M_{14}, averaged over orientation. During averaging, the mutual arrangement of particles within the cluster was preserved.

Significant values of CIDS, expressed through $-M_{14}/M_{11}$, were obtained for all particle types. However, it is important to note that for asymmetrically arranged, symmetric shapes, such as spheres and capsules, which do not generate circular polarization when scattered as single particles, the dependence of CIDS on the scattering angle exhibits oscillations around zero. The statistical characteristics of these oscillations, which are already small when arithmetically averaged over all scattering angles, diminish in amplitude as the interparticle distance and the number of particles increase. In contrast, only for clusters of chiral helices does a significant trend emerge, which remains relatively stable with respect to the distance between particles, but becomes more flattened as the number of particles increases.

Similar characteristics of the CIDS signal, manifested as a picket-fence pattern of oscillations around zero and the formation of more defined curves with pronounced slopes for particles containing a chiral biological component, have also been indirectly confirmed in experimental studies of CIDS. These studies include light scattering from nearly symmetric polystyrene latex (PSL) microspheres and various biological objects such as PSL spheres doped with DNA molecules, bacterial spores, or pollen [5,36]. Although the underlying mechanisms may differ, they could be attributed to factors such as positioning errors of the particles in an optical trap or during their transit through the detector.

Author Contributions: Conceptualization, Y.S. (Yehor Surkov) and G.V.; methodology, Y.S. (Yehor Surkov), K.M., A.P., Y.H., C.W., Y.-L.P., G.V., V.K. and Y.S. (Yuriy Shruratov); software, Y.S. (Yehor Surkov); validation, Y.S. (Yehor Surkov); formal analysis, Y.S. (Yehor Surkov); investigation, Y.S. (Yehor Surkov), K.M., A.P., Y.H., C.W., Y.-L.P., G.V., V.K. and Y.S. (Yuriy Shkuratov); resources, Y.S. (Yehor Surkov); data curation, Y.S. (Yehor Surkov); writing—original draft preparation, Y.S. (Yehor Surkov) and G.V.; writing—review and editing, Y.S. (Yuriy Shkuratov), K.M., A.P., Y.H., C.W., Y.-L.P., G.V. and V.K.; visualization, Y.S. (Yehor Surkov); supervision, K.M., A.P. and G.V.; project administration, K.M. and G.V.; funding acquisition, K.M., Y.H. and G.V. All authors have read and agreed to the published version of the manuscript.

Funding: Yehor Surkov, Karri Muinonen, and Antti Penttilä were supported by the Research Council of Finland grants No. 336546 and 359893. Yongxiang Hu and Gorden Videen were supported in part by the NASA Interdisciplinary Research in Earth Science NNH22ZDA001N-IDS, grant 80NSSC24K0851.

Data Availability Statement: Dataset available on request from the authors.

Acknowledgments: During the preparation of this manuscript/study, the non-native English speaker authors used Grammarly for the purpose of language editing. The authors have reviewed and edited the output and take full responsibility for the content of this publication.

Conflicts of Interest: The authors declare no conflicts of interest.

Abbreviations

The following abbreviations are used in this manuscript:

LP	Linear Polarization
CIDS	Circular intensity differential scattering
LDR	Lattice Dispersion relation
RMSD	Root mean square deviation

References

1. Bickel, W.S.; Stafford, M.E. Polarized light scattering from biological systems: A technique for cell differentiation. *J. Biol. Phys.* **1981**, *9*, 53–56. [CrossRef]
2. Shapiro, D.B.; Hunt, A.J.; Quinby-Hunt, M.S.; Hull, P.G.; Spinard, R.W. Circular polarization effects in the light scattering from single and suspensions of dinoflagellates. In *Underwater Imaging, Photography, and Visibility*; SPIE: Bellingham, WA, USA, 1991; Volume 1537, pp. 30–41. [CrossRef]
3. Kunnen, B.; Macdonald, C.; Doronin, A.; Jacques, S.; Eccles, M.; Meglinski, I. Application of circularly polarized light for non-invasive diagnostics of cancerous tissues and turbid tissue-like scattering media. *J. Biophotonics.* **2014**, *8*, 317–323. [CrossRef]
4. Gassó, S.; Knobelspiesse, K.D. Circular polarization in atmospheric aerosols. *Atmos. Chem. Phys.* **2022**, *22*, 13581–13605. [CrossRef]
5. Pan, Y.L.; Kalume, A.; Beresnev, L.; Wang, C.; Kinahan, S.; Rivera, D.N.; Crown, K.K.; Santarpia, J. Rapid bioaerosol detection by measuring circular intensity differential scattering (CIDS) from single flowing through particle. *Aerosol Sci. Technol.* **2024**, *58*, 91–98. [CrossRef]
6. Ackerman, D.; Pan, Y.L.; Kalume, A.; Klug, E.; Ravnholdt, A.; Crown, K.; Santarpia, J. The impact of environmental aging processing on bioaerosol detection using circular intensity differential scattering (CIDS). *J. Aerosol Sci.* **2025**, *186*, 106555. [CrossRef]
7. Berdyugina, S.; Kuhn, J.; Harrington, D.; Santl-Temkiv, T.; Messersmith, J. Remote sensing of life: Polarimetric signatures of photosynthetic pigments as sensitive biomarkers. *Internat. J. Astrobiol.* **2016**, *15*, 45–56. [CrossRef]
8. Patty, C.H.L.; ten Kate, I.L.; Buma, W.J.; van Spanning, R.J.M.; Steibach, G.; Ariese, F.; Shik, F. Circular spectropolarimetric sensing of vegetation in the field: Possibilities for the remote detection of extraterrestrial life. *Astrobiology* **2019**, *19*, 1221–1229. [CrossRef]
9. Patty, C.H.L.; Kühn, J.G.; Lambrev, P.H.; Spadaccia, S.; Hoeijmakers, H.J.; Keller, C.; Mulder, W.; Pallichadath, V.; Poch, O.; Snik, F.; et al. Biosignatures of the Earth, I. Airborne spectropolarimetric detection of photosynthetic life. *Astron. Astrophys.* **2021**, *651*, A68. [CrossRef]
10. Rosenbush, V.; Kolokolova, L.; Lazarian, A.; Shakhovskoy, N.; Kiselev, N. Circular polarization in comets: Observations of Comet C/1999 S4 (LINEAR) and tentative interpretation. *Icarus* **2007**, *186*, 317–330. [CrossRef]
11. Rosenbush, V.; Kiselev, N.; Kolokolova, L. Predominantly left-handed circular polarization in comets: Does it indicate L-enantiomeric excess in cometary organics? *Proc. Int. Astron. Union* **2008**, *4*, 311–312. [CrossRef]
12. Hulst, H.C.; van de Hulst, H.C. *Light Scattering by Small Particles*; Dover: New York, NY, USA, 1981; p. 470.
13. Mishchenko, M.I.; Travis, L.D.; Lacis, A. *Scattering, Absorption, and Emission of Light by Small Particles*; Cambridge University Press: Cambridge, UK, 2002; p. 486.
14. Kolokolova, L.; Kimura, H.; Zieger, K.; Mann, I. Light-scattering properties of random-oriented aggregates: Do they represent the properties of an ensemble of aggregates? *J. Quant. Spectrosc. Radiat. Transf.* **2006**, *100*, 199–206. [CrossRef]
15. Kolokolova, L.; Sparks, W.B.; Mackowski, D.W. Astrobiological remote sensing with circular polarization. In *Polarimetric Detection, Characterization, and Remote Sensing*; Mishchenko, M.I., Yatskiv, Y.S., Rosenbush, V.K., Videen, G., Eds.; Springer: Berlin/Heidelberg, Germany, 2011; pp. 277–294.
16. Nagdimunov, L.; Kolokolova, L.; Mackowski, D. Characterization and remote sensing of biological particles using circular polarization. *J. Quant. Spectrosc. Radiat. Transf.* **2013**, *131*, 59–65. [CrossRef]

17. Guirado, D.; Hovenier, J.W.; Moreno, F. Circular polarization of light scattered by asymmetrical particles. *J. Quant. Spectrosc. Radiat. Transf.* **2007**, *106*, 63–73. [CrossRef]
18. Guirado, D.; Moreno, F.; Hovenier, J.W. Circular polarization of light scattered by randomly built aggregates. In Proceedings of the 10th Conference on Electromagnetic and Light Scattering, Bodrum, Turkey, 17–22 June 2007; pp. 45–48. [CrossRef]
19. Drachev, V.; Bragg, W.; Podolskiy, V.; Safonov, V.; Kim, W.T.; Ying, C.; Armstrong, R.; Shalaev, V. Large local optical activity in fractal aggregates of nanoparticles. *J. Opt. Soc. Am. B* **2001**, *18*, 1896–1903. [CrossRef]
20. Sparks, W.; Hough, J.; Germer, T.; Chen, F.; DasSarma, S.; DasSarma, P.; Robb, F.; Manset, N.; Kolokolova, L.; Reid, N.; et al. Detection of circular polarization in light scattered from photosynthetic microbes. *Proc. Natl. Acad. Sci. USA* **2009**, *106*, 7816–7821. [CrossRef] [PubMed]
21. Kolokolova, L.; Koenders, C.; Goetz, C.; Rosenbush, V.; Kiselev, N.; Hoang, T.; Lazarian, A. Clues to cometary circular polarization from studying the magnetic field in the vicinity of the nucleus of comet 67P/Churyumov-Gerasimentko. *Mon. Not. R. Astron. Soc.* **2016**, *462*, 422–431. [CrossRef]
22. Teitelbaum, C.S.; Ferraz, A.; De La Cruz, S.E.W.; Gilmour, M.E.; Brosnan, I.G. The potential of remote sensing for infectious disease ecology research and practice. *Proc. Biol. Sci.* **2024**, *291*, 20241712. [CrossRef]
23. Santarpia, J.L.; Reid, J.P.; Wu, C.-Y.; Lednicky, J.A.; Oswin, H.P. The aerobiological pathway of natural respiratory viral aerosols. *TrAC Trends Anal. Chem.* **2024**, *172*, 117557. [CrossRef]
24. Molina, B.J.; Rossi, L.; Stam, D.M. Traces of exomoons in computed flux and polarization phase curves of starlight reflected by exoplanets. *Astron. Astrophys.* **2018**, *618*, A162. [CrossRef]
25. Rossi, L.; Stam, D.M. Circular polarization signals of cloudy (exo)planets. *Astron. Astrophys.* **2018**, *616*, A117. [CrossRef]
26. Bohren, C.F.; Huffman, D.R. *Absorption and Scattering of Light by Small Particles*; Wiley: Hoboken, NJ, USA, 2004; p. 530.
27. Surkov, Y.; Shkuratov, Y.; Pan, Y.L.; Kalume, A.; Santarpia, J.; Zubko, E.; Hu, Y.; Videen, G. Light scattering from spiral particles. *J. Quant. Spectrosc. Radiat. Transf.* **2023**, *298*, 108494. [CrossRef]
28. Draine, B.T.; Flatau, P.J. The discrete dipole approximation for scattering calculations. *J. Opt. Soc. Am. A* **1994**, *11*, 1491–1499. [CrossRef]
29. Yurkin, M.; Hoekstra, A. The discrete-dipole-approximation code ADDA: Capabilities and known limitations. *J. Quant. Spectrosc. Radiat. Transf.* **2011**, *112*, 2234–2247. [CrossRef]
30. Yurkin, M.A.; Hoekstra, A.G. User Manual for the Discrete Dipole Approximation Code ADDA 1.4.0. Available online: https://github.com/adda-team/adda/raw/v1.4.0/doc/manual.pdf (accessed on 10 October 2025).
31. Yurkin, M.A.; Hoekstra, A.G. The discrete dipole approximation: An overview and recent developments. *J. Quant. Spectrosc. Radiat. Transf.* **2007**, *106*, 558–589. [CrossRef]
32. Fu, R.; Wang, C.; Muñoz, O.; Videen, G.; Santarpia, J.; Pan, Y.L. Elastic back-scattering patterns via particle surface roughness and orientation from single trapped airborne aerosol particles. *J. Quant. Spectrosc. Radiat. Transf.* **2017**, *187*, 224–231. [CrossRef]
33. Pan, Y.L.; Wang, C.; Beresnev, L.; Yuffa, A.; Videen, G.; Ligon, D.; Santarpia, J. Measurement of back-scattering patterns from single laser trapped aerosol particles in air. *Appl. Opt.* **2017**, *56*, B1–B4. [CrossRef] [PubMed]
34. Zubko, E.; Shkuratov Yu Videen, G.; Kiselev, N.N. DDA simulations of light scattering by small irregular particles with various structure. *J. Quant. Spectrosc. Radiat. Transf.* **2006**, *101*, 416–434. [CrossRef]
35. Surkov, Y.; Shkuratov, Y.; Kaydash, V.; Pan, Y.L.; Kalume, A.; Heinson, Y.; Wang, C.; Hu, Y.; Videen, G. Lights scattering be droplets containing small chiral particles. *J. Quant. Spectrosc. Radiat. Transf.* **2025**, *346*, 109604. [CrossRef]
36. Alali, H.; Pan, Y.L.; Kalume, A.; Hu, Y.; Surkov, Y.; Shkuratov, Y.; Videen, G.; Wang, C. Measurement of circular intensity differential scattering (CIDS) from single optically trapped biological particles. *J. Quant. Spectrosc. Radiat. Transf.* **2025**, *330*, 109244. [CrossRef]

Disclaimer/Publisher's Note: The statements, opinions and data contained in all publications are solely those of the individual author(s) and contributor(s) and not of MDPI and/or the editor(s). MDPI and/or the editor(s) disclaim responsibility for any injury to people or property resulting from any ideas, methods, instructions or products referred to in the content.